J. Fluid Mech. (2025), *vol.* 1011, A14, doi:10.1017/jfm.2025.391

JFM PAPERS

Experimental study of velocity statistics in wall-bounded turbulent emulsions

Yaning Fan[1,†], **Yi-Bao Zhang**[1,†], **Jinghong Su**[1], **Lei Yi**[1,2],
Cheng Wang[1,3] **and Chao Sun**[1,4]

[1]New Cornerstone Science Laboratory, Center for Combustion Energy, Key Laboratory for Thermal Science and Power Engineering of Ministry of Education, Department of Energy and Power Engineering, Tsinghua University, Beijing 100084, PR China

[2]Department of Physics, University of Massachusetts, Amherst, MA 01003, USA

[3]ENS de Lyon, CNRS, Laboratoire de physique, Lyon F-69342, France

[4]Department of Engineering Mechanics, School of Aerospace Engineering, Tsinghua University, Beijing 100084, PR China

Correspondence author: Chao Sun, chaosun@tsinghua.edu.cn

(Received 14 October 2024; revised 31 March 2025; accepted 4 April 2025)

Turbulent emulsions are ubiquitous in chemical engineering, food processing, pharmaceuticals and other fields. However, our experimental understanding of this area remains limited due to the multiscale nature of turbulent flow and the presence of extensive interfaces, which pose significant challenges to optical measurements. In this study, we address these challenges by precisely matching the refractive indices of the continuous and dispersed phases, enabling us to measure local velocity information at high volume fractions. The emulsion is generated in a turbulent Taylor–Couette flow, with velocity measured at two radial locations: near the inner cylinder (boundary layer) and in the middle gap (bulk region). Near the inner cylinder, the presence of droplets suppresses the emission of angular velocity plumes, which reduces the mean azimuthal velocity and its root mean squared fluctuation. The former effect leads to a higher angular velocity gradient in the boundary layer, resulting in greater global drag on the system. In the bulk region, although droplets suppress turbulence fluctuations, they enhance the cross-correlation between azimuthal and radial velocities, leaving the angular velocity flux contributed by the turbulent flow nearly unchanged. In both locations, droplets suppress turbulence at scales larger than the average droplet diameter and increase the intermittency of velocity increments. However, the effects of the droplets are more pronounced near the inner cylinder than in the bulk, likely because droplets fragment in the boundary layer but are less prone to break up in the bulk. Our study provides experimental insights into how dispersed droplets modulate global drag, coherent structures and the multiscale characteristics of turbulent flow.

[†] Yaning Fan, Yi-Bao Zhang contributed equally to this work.

Key words: emulsions, Taylor-Couette flow, multiphase flow

---

1. Introduction

Emulsions, consisting of two immiscible liquids, are ubiquitous in various natural and industrial processes, such as oil spills in the ocean, pharmaceuticals, food processing, oil production and recovery (Li & Garrett 1998; McClements 2004; Kokal 2005; Spernath & Aserin 2006; Gopalan & Katz 2010; Mandal *et al.* 2010; Kilpatrick 2012). In turbulent emulsions, the multiscale nature of turbulence adds to the complexity of the system. Therefore, although emulsions are frequently encountered, our understanding of the underlying physics of emulsions, particularly turbulent emulsions, remains elementary.

Two major unanswered questions in the study of emulsions pertain to (i) droplet dynamics (the droplet size distribution and preferential concentration of droplets in certain regions of the flow) and (ii) the modulation of the statistics of the base flow. The investigation on droplet size in turbulent flow can be traced back to Kolmogorov (1949) and Hinze (1955). In their theory, the background turbulence is assumed to be homogeneous and isotropic, with the maximum droplet size, d_H, determined by the competition between turbulent fluctuations induced external pressure force from the background flow over the droplet and resisting capillary cohesive forces of the droplets (Risso & Fabre 1998; Perlekar *et al.* 2012; Perlekar *et al.* 2014; Eskin, Taylor & Yang 2017; Rosti *et al.* 2019; Begemann *et al.* 2022). However, it has been pointed out that the Kolmogorov–Hinze theory has certain limitations, particularly in non-homogeneous turbulent flows (Hinze 1955; Lemenand *et al.* 2017). Recent studies on wall-bounded Taylor–Couette (TC) turbulence (Yi *et al.* 2022) suggest that the average droplet size in the bulk region is not governed by the Kolmogorov–Hinze model (Kolmogorov 1949; Hinze 1955), but instead by the dynamic pressure induced by the gradient of the mean flow, as proposed by Levich (Levich 1962). For more details on the breakup of bubbles and droplets in turbulence, we refer to the review paper by Ni (2024) and the references therein.

In turn, the presence of droplets can also alter the statistical properties of turbulence and the global transport quantities, such as drag, in the emulsion (Piela *et al.* 2008; Yi, Toschi & Sun 2021). Yi *et al.* (2021, 2022) and Wang *et al.* (2022*b*) found that the size and viscosity of the droplets have a profound effect on the global drag of the system. The drag increases with the volume fraction and viscosity of the dispersed phase, and the effective viscosity of the emulsion system exhibits a shear-thinning effect as the shear increases. Bakhuis *et al.* (2021) and Yi *et al.* (2024) studied catastrophic phase inversion in turbulent TC flow, demonstrating that significant drag reductions in the transport of emulsions can be achieved by selecting the appropriate emulsion type. The modulation of turbulence by the presence of droplets in turbulent emulsions has recently attracted growing interest in numerical simulations. For small-scale statistics, Crialesi-Esposito *et al.* (2022) analysed velocity and vorticity fluctuations and observed a significant deviation in the tails of probability density functions (PDFs). The observation that a deformable interface increases intermittency has been further verified, with the effect primarily attributed to the strong velocity differences across the interfaces (Crialesi-Esposito *et al.* 2023*a*). For large-scale modulation, Hori *et al.* (2023) reported two regimes in TC emulsion at a Reynolds number of 960 based on the Weber number: an advection-dominated regime and an interface-dominated regime, where both the global drag and Taylor roll structures are strongly modulated. More specifically, Dodd & Ferrante (2016) and Perlekar (2019) examined the turbulent kinetic energy (TKE) budget for varying

Weber numbers in homogeneous isotropic turbulence. Both studies found that the total kinetic energy compensates for surface area variations; i.e. the presence of interfaces introduces an alternative kinetic energy transfer mechanism, with TKE decreasing as the interface increases, and *vice versa*. Trefftz-Posada & Ferrante (2023) conducted a similar investigation in homogeneous shear turbulence, analysing production, dissipation and surface tension terms separately to study their modulation effects on TKE. They proposed 'catching-up' mechanisms to explain the higher degree of enhancement of production and dissipation rate of TKE for lower Weber number case.

From the above, it is clear that most experimental studies were conducted on the global properties of emulsions when concerned about system modulations, and our knowledge of turbulence modulation by droplets based on experiments is limited. Experimental techniques using optical measurements have been widely applied in fluid dynamics to provide detailed velocity information with high spatial and temporal resolution. However, a major challenge arises for optical measurements in multiphase flows, especially emulsions, because the emulsion fluid is opaque due to the presence of liquid–liquid interfaces. This is illustrated in figure 1(*a*), where a ruler is immersed in the fluid as a reference. Although the dispersed and continuous phases are individually transparent, their mixture is not. The small droplets in the emulsion system act as spherical lenses. When a light beam passes through the mixture, it experiences multiple reflections and refractions (see figure 1*b*), making the ruler difficult to see and rendering optical measurements unfeasible. In light of this challenge, previous optical measurements in liquid–liquid flows were primarily conducted under stratified conditions, at low Reynolds numbers, or at low volume fractions of the dispersed phases (Conan *et al.* 2007; Kumara, Halvorsen & Melaaen 2010; Morgan *et al.* 2013; Ibarra *et al.* 2018, 2021; Yi *et al.* 2023). Thus, our experimental understanding of the underlying mechanisms of turbulence modulation in turbulent emulsions remains limited, particularly at high dispersed volume fractions.

In this work, we address this challenge by precisely matching the refractive indices of the dispersed and continuous phases and experimentally investigating the mechanisms of drag and turbulence modulation by the dispersed droplets. This paper is organised as follows. In § 2, we introduce the experimental set-up, the unique preparation of working fluids and the methodology utilised in detail. In § 3, we present the major results, including the global drag modulation and the modification of the continuous phase at two radial positions. Finally, in § 4, we conclude the paper with a brief summary and outlook.

2. Experimental set-up and methodology

2.1. *Experimental set-up*

Taylor–Couette turbulence, which refers to the flow between two coaxial cylinders, is one of the classic systems in fluid mechanics. The TC is a closed system that allows for precise control of the volume fraction of the dispersed phase and features easy accessibility for global drag and local velocity measurements. In our experiments, the TC system is constructed from a commercial rheometer (Discovery Hybrid Rheometer, TA Instruments), as shown in figure 1(*e*). The system consists of an inner cylinder with a radius $r_i = 25$ mm and height $L = 100$ mm, and an outer cylinder with a radius $r_o = 35$ mm and height 110 mm. These two cylinders create a gap $d = r_o - r_i = 10$ mm, a radius ratio $r_i/r_o = 0.714$ and an aspect ratio $\Gamma = L/d = 10$. The inner cylinder is made of aluminium and anodized to form a black oxidation layer, which reduces unwanted reflection that could decrease the signal-to-noise ratio during optical measurements. The outer cylinder and the cubic tank, which encloses the outer cylinder, are made of Plexiglass, allowing for optical

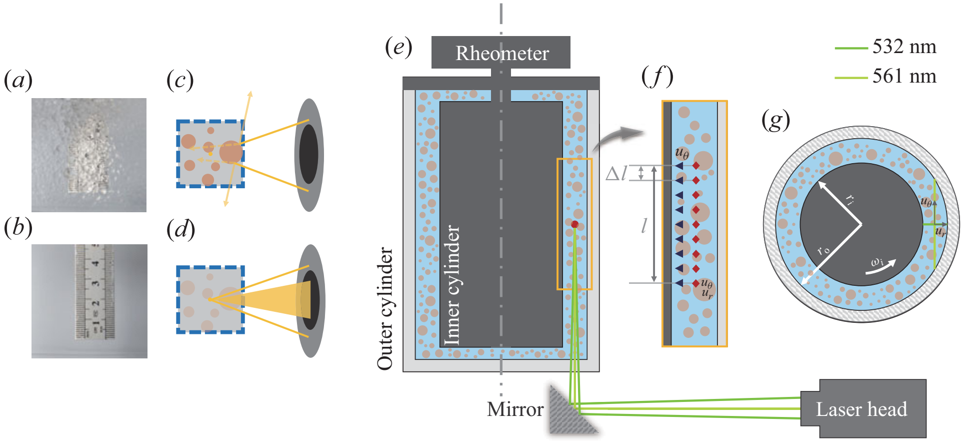

Figure 1. A picture of a ruler immersed in an emulsion fluid before (*a*) and after (*b*) refractive index matching. The cartoon illustrates the laser Doppler anemometer (LDA) measurements before (*c*) and after (*d*) refractive index matching. We note that in (*d*), the light brown circles are included to remind the reader that the flow system consists of droplets, which are not actually visible. (*e*) A sketch of the experimental set-up, with the measurement technique LDA also depicted. (*f*) An enlarged view of the LDA measurement location: the blue triangles represent measurement points near the inner cylinder, while the red diamonds represent points in the middle gap. (*g*) A cross-section of the TC system, with the inner and outer cylinder radii denoted as r_i and r_o, respectively. The measured velocity components in the azimuthal and radial directions are denoted as u_θ and u_r, respectively. We note that the circles are shown to remind the reader that liquid–liquid two-phase turbulence is being investigated here; these droplets cannot actually be seen.

accessibility. The upper cover is made of black acrylonitrile butadiene styrene to further minimise unwanted reflection from above.

The inner cylinder is directly screwed onto the rheometer and driven by its motor at a constant angular velocity ω_i. The outer cylinder, associated with the cubic tank, is fixed. The global torque required to maintain a constant ω_i can be directly measured by the rheometer, with high accuracy of up to 0.1 nN m. The time series of torque is recorded after a statistically steady state is reached. The measured torque consists of two parts: one contributed by the TC flow and the other originating from the top and bottom end plates (von Kármán flow). The latter contribution can be estimated using the same linearisation method that has been fully discussed in our previous studies (Wang *et al.* 2022*a*; Yi *et al.* 2022). The torque contributed by the TC flow is denoted as T in the following.

The control parameter of the TC system is the Reynolds number defined as

$$Re = \omega_i r_i d/\nu_c, \tag{2.1}$$

where $\nu_c = \mu_c/\rho_c$ is the kinematic viscosity of the continuous phase. ν, μ and ρ are the kinematic viscosity, dynamics viscosity and density of the fluid. We use subscripts c and d to discriminate the continuous and dispersed phase. For the two-phase case, volume fraction of the dispersed phase ϕ is needed. A key response parameter of the system is the dimensionless torque defined as

$$G = T/(2\pi L\rho_c \nu_c^2). \tag{2.2}$$

2.2. *Working fluid*

As mentioned in the introduction, the presence of a two-phase interface typically makes the fluid optically opaque, which greatly limits the applicability of optical measurements. To address this issue, we precisely match the refractive index between the continuous and dispersed phases (see review articles Budwig (1994), Wiederseiner *et al.* (2011), Amini & Hassan (2012) and Wright, Zadrazil & Markides (2017)). After refractive index matching, the droplets are invisible within the continuous phase, making the entire emulsion system optically transparent, as sketched in figure 1(*c,d*).

In this work, the continuous phase is a mixture of ultrapure water (density $\rho_w = 0.998 \times 10^3$ kg m^{-3}, refractive index $n_w = 1.3325$) and glycerol (Titan Greagent, G66258A, $\rho_g = 1.231 \times 10^3$ kg m^{-3}, $n_g = 1.4720$). The dispersed phase is a mixture of silicone oil (Shin–Etsu KF-96L-2cSt, $\rho_s = 0.873 \times 10^3$ kg m^{-3}, $n_s = 1.391$) and ethoxy-nonafluorobutane (Novec 7200 3M, $\rho_n = 1.420 \times 10^3$ kg m^{-3}, $n_n = 1.3014$). Here, n denotes the refractive index of the fluid. To match the refractive index, we first estimate the volume fraction of the ith component, φ_i, according to the classic Newtons equation (Newton 1704; Kurtz Jr & Ward 1936; Reis *et al.* 2010),

$$n_{12}^2 = \varphi_1 n_1^2 + \varphi_2 n_2^2, \tag{2.3}$$

where n_i is the refractive index for the ith component and n_{12} is for the mixture. We measure the refractive indices of the continuous and dispersed phases, n_c and n_d, using a commercial refractometer (GR30, Shanghai Zhuoguang Instrument Technology Co., Ltd.) with a resolution of 0.0001 and an accuracy of ±0.0002 at a temperature of 25 °C, which is the temperature of the emulsion during the experiment. We then compare n_c and n_d and carefully adjust $\varphi_{1,2}$ until $n_c = n_d$ within the precision of the refractometer. It is important to note that even the addition of 0.1 g of silicone oil or Novec 7200 to a 200 g mixture of oil and Novec 7200 will alter its refractive index. Additionally, the densities of the two phases must also be matched to eliminate the effect of centrifugal force (Yi *et al.* 2021). If the densities are not matched, we have to adjust the target refractive index and repeat the procedure described above until both refractive index matching and density matching are satisfied. The volume fractions of each fluid for the continuous phase are $\phi_w \approx 87.9\,\%$ and $\phi_g \approx 12.1\,\%$, and those for the dispersed phase are $\phi_s \approx 65.9\,\%$ and $\phi_n \approx 34.1\,\%$.

Consequently, the water–glycerol (W–G) mixture, as the continuous phase, has a density of $\rho_c = 1.033 \times 10^3$ kg m^{-3}, kinematic viscosity of $\nu_c = 1.26 \times 10^{-6}$ m^2 s^{-1} and refractive index of $n_c = 1.3506$. The silicon-oil–Novec (O–N) mixture, as the dispersed phase, has $\rho_d = 1.046 \times 10^3$ kg m^{-3}, $\nu_d = 1.15 \times 10^{-6}$ m^2 s^{-1} and $n_d = 1.3506$. The interfacial tension of the two phases is calculated based on the equation proposed by Girifalco & Good (1957) for solid–liquid systems, which is equally valid for liquid–liquid systems (Lee 1993)

$$\gamma = \gamma_c + \gamma_d - 2\zeta(\gamma_c\gamma_d)^{1/2}, \tag{2.4}$$

where γ_c (γ_d) is the surface tension of the continuous (dispersed) phase, and γ is the interfacial tension between the two phases. Here ζ is the interfacial interaction parameter, set to a value of 1. The values of $\gamma_c = 73.28 \times 10^{-3}$ N m^{-1} and $\gamma_d = 15.73 \times 10^{-3}$ N m^{-1} are measured in air using the pendant drop method. The interfacial tension between W–G and O–N is $\gamma = 21.11 \times 10^{-3}$ N m^{-1}. In turbulent emulsions, dynamic pressure and viscous stress deform and break up the droplets, while interfacial tension resists deformation. The effect of dynamic pressure is measured by Weber number of the system (Crialesi-Esposito *et al.* 2023*b*; Hori *et al.* 2023; Su *et al.* 2024*a*,*b*, 2025), defined as $We_{sys} = \rho_c u_\tau^2 d/\gamma$, is $We_{sys} = 4$. Here, $u_\tau = \sqrt{T/(2\pi r_i^2 L\rho_c)}$ is the friction velocity. The effect of viscous stress can be measured by the capillary number $Ca = \tau_\nu/\tau_\gamma = \nu\rho_c\epsilon^{1/2}D/(\gamma\nu^{1/2})$, where the average energy dissipation rate ϵ is estimated from the global torque $\epsilon \approx 0.1T\omega_i/(\pi(r_o^2 - r_i^2)L\rho_c)$ (Ezeta *et al.* 2018; Yi *et al.* 2022). In our study, the capillary number is approximately 0.01, which is much smaller than 1. Therefore, viscous stress is not important in determining the droplet deformation and breakup.

2.3. *Velocity measurement in the continuous phase*

We employ a LDA (TSI) to measure velocity due to its high temporal and spatial resolution. The LDA consists of two pairs of laser beams, with wavelengths of 561 nm and 532 nm, as shown in figure 1(*e*–*g*). We use the 561 nm and 532 nm laser beams to measure the azimuthal and radial velocity components, denoted as u_θ and u_r, respectively (see figure 1(*g*)). The beam waist diameter and length of the measurement volume are around 260 μm and 3.2 mm, respectively. The physical size of the LDA measurement volume will not affect the measured data and the details are discussed in Appendix B. The laser head of the LDA is mounted on a high-precision platform, which can move independently in the x, y and z directions. It consists of two parts: a vertical electric lifting table (Fly-opt, PSTV50-S57) with a precision of 20 μm and a maximum stroke of 50 mm, and an x–y electric horizontal displacement table (RedStarYang EPSB-150-B-G and EPSB-50-B-G) with precisions of 20 μm and 10 μm, and maximum strokes of 150 mm and 50 mm in the x and y directions, respectively. This platform allows us to change the measurement location. A 45° mirror is used to reflect the laser beam to pass through the TC system from below. In this way, distortion of the laser beam due to the curved outer cylinder can be avoided (Huisman *et al.* 2012*b*). The seeding particles used are polystyrene (Ruige Tech.) with an average diameter of 5 μm and a density of 1.05×10^3 kg m^{-3}. The surfaces of the polystyrene particles are grafted with hydroxyl groups to make them hydrophilic. Thus, the particles can only dissolve in the continuous phase, whose velocity information can be measured by the LDA.

In LDA measurements, a slight mismatch in the refractive index or variation in temperature from 25 °C can cause the data rate to drop sharply. Therefore, precisely matching the refractive index and controlling the temperature are crucial. Temperature-controlled water from a refrigerator is circulated between the outer cylinder and the cubic tank. A PT100 thermocouple is used to measure the temperature of the emulsion, with its variation from 25 °C remaining within 0.1 °C during the experiment. We also finely tune the concentration of the seeding particles to ensure that the data rate of the LDA in both single-phase and two-phase measurements is as close as possible.

The TC flow can be divided into two parts: the boundary layer near the inner and outer cylinder where there exist high velocity gradient, and the bulk region where the flow is nearly homogeneous and isotropic (Grossmann, Lohse & Sun 2016). Therefore, in our experiments the velocity measurements are performed at two representative locations in the radial direction: near the inner cylinder and at the middle gap. In the former case, the dimensionless distance from the inner cylinder is given by $\tilde{r} = (r - r_i)/(r_o - r_i) = 0.05$, and in terms of the viscous length scale, $y^+ = (r - r_i)/(\delta_\nu) \approx 35$ (Huisman *et al.* 2013*b*). The viscous length δ_ν is defined as $\delta_\nu = \nu_c/\sqrt{T/(2\pi r_i^2 L \rho_c)}$. It is based on the properties of continuous phase considering the minor differences between two phases. The torque T used for δ_ν estimation is taken from the single-phase case since the global drag is only slightly enhanced. In the latter case, the dimensionless distance from the inner cylinder is $\tilde{r} = 0.5$. At the middle gap, both u_θ and u_r are measured, while only u_θ can be obtained near the inner cylinder due to the obstruction of the laser beam by the bottom end of the inner cylinder. For each radial position, by adjusting the location of the laser head every 2 mm, LDA measurements are taken at 10 different heights, separated by $\Delta l \approx 2.70$ mm due to the difference in refractive indices of air and the working fluid. The axial length of one pair of Taylor vortices is around $2.1d$ (Zhang *et al.* 2025). Thus, velocity data at nine axial heights, spanning a length of $l \approx 21.63$ mm $\approx 2.1d$, are used with their centre located at the middle height of the TC set-up. In this way the influence of secondary flow can be minimised. For the LDA technique we use in this work, the total amount of data points acquired once can be set in the software. Near the inner cylinder, a fixed amount of data points of 5×10^5 is acquired since only u_θ is collected. While at the middle gap, the total amount of data points for two velocity components is set to be 1×10^6. The actual number of data points for u_θ and u_r is determined by the average sampling frequency, i.e. data rate, while the total measurement time is the same. Higher sampling frequency in one direction, more data points in that direction and fewer in the other. However, since the data rates of two components are quite close, the number of data points in both directions is approximately 5×10^5. In this way, the velocity components u_θ and u_r of the continuous phase, which are functions of vertical position z and time t, can be obtained. The details of preprocessing of velocity time series are introduced in Appendix B. Since TC turbulence is statistically steady, the velocity components can be decomposed into the mean and fluctuation parts. Taking u_θ as an example, $u_\theta = \langle u_\theta \rangle_t + u'_\theta$, where $\langle\ \rangle_t$ denotes averaging over time. In TC turbulence, due to the presence of Taylor vortices, turbulence statistics depend on the vertical position. We thus also perform an additional average in the z direction, i.e. $\langle u_\theta \rangle_{t,z}$. The root mean squared (r.m.s.) fluctuation of u_θ is defined as $\sigma(u'_\theta) = \langle \sqrt{\langle u'^2_\theta \rangle_t} \rangle_z$.

To measure the droplet size, Oil Red O (MCE) is dissolved in the droplets to make them visible. The illumination of the droplets is achieved through backlighting, and their images are captured by a high-speed camera (Photron NOVA S12) equipped with a microlens. Considering that the size of the droplets and the measurement window are much smaller than the diameter of the outer cylinder, the distortion of the droplet image due to curvature can be neglected (Yi *et al.* 2021). The average droplet size is computed from approximately 10^3 droplets. We conduct the diameter measurement at $\mathrm{Re} = 1.68 \times 10^4$ with a volume fraction $\phi = 1\,\%$ in the bulk region of TC flow. We use the symbol $\langle D \rangle$ to denote the mean diameter, which is $\langle D \rangle \approx 700$ µm. Further discussions on the mean droplet size and its radial dependence are included in Appendix A.

3. Results and discussion

The dimensionless torque of the inner cylinder defined in (2.2) for different O–N volume fractions, ϕ, and Reynolds number, Re, is depicted in figure 2. We also compare our results with previous study (Yi *et al.* 2021), shown as dashed–dotted line in figure 2. It is found that G increases with ϕ for a fixed Re, consistent with our previous studies (Yi *et al.* 2021, 2022; Wang *et al.* 2022*b*). Note that the slope of G obtained in previous work is different from the current one. This may be caused by the different interfacial tension, which would influence the droplet size and its distribution. According to Su *et al.* (2024*b*), the interface contribution to the drag is a function of interfacial tension and curvature of the droplet interface. The increase of the global drag signifies that the turbulent flow is modified by the presence of droplets, not only the global transportation but also the local flow statistics, such as the mean velocity and r.m.s. velocity fluctuation. In the following, we reveal how droplets modulate the drag and the turbulence of the continuous phase.

3.1. *Modulation of continuous phase near the inner wall*

We start with the turbulence statistics near the inner cylinder ($\tilde{r} = 0.05$, $y^+ = 35$), where only the azimuthal velocity is measured as depicted in figure 3(*a*). The average velocity $\langle u_\theta \rangle_{t,z}$ as well as r.m.s. fluctuation $\sigma(u'_\theta)$ with varying O–N volume fraction ϕ at two

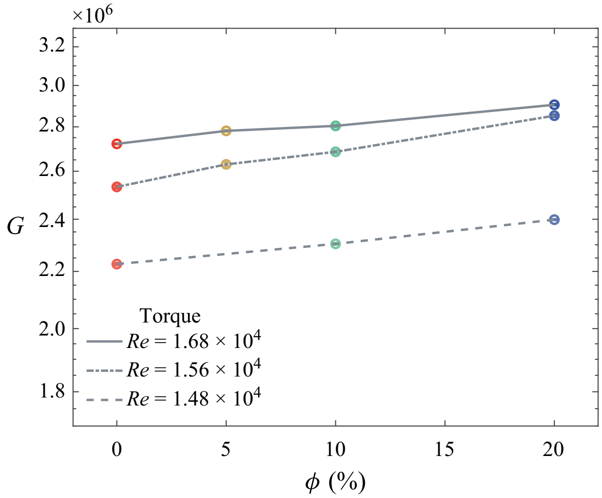

Figure 2. The dimensionless torque, G, is presented as a function of the volume fraction of the dispersed phase for three different Reynolds numbers, Re. The datasets at $Re = 1.68 \times 10^4$ and $Re = 1.48 \times 10^4$ are measured in this work, while the dataset at $Re = 1.56 \times 10^4$ is from Yi *et al.* (2021).

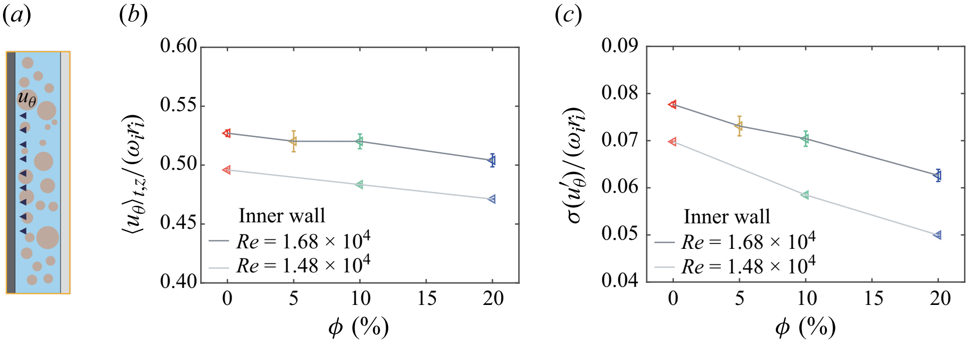

Figure 3. (*a*) The schematic shows the LDA measurement positions near the inner cylinder, represented by the blue triangles. Only the azimuthal velocity u_θ can be measured here due to the shielding of the laser beams by the inner cylinder. Average velocity (*b*) and r.m.s. velocity fluctuation (*c*) of u_θ are presented with varying volume fraction ϕ for two Reynolds numbers. Both $\langle u_\theta \rangle_{t,z}$ and $\sigma(u'_\theta)$ are normalised by the velocity of the inner cylinder.

different Reynolds numbers Re are shown in figure 3(*b*,*c*). Note that the error bars are calculated based on the following steps: we first use bootstrap method to calculate the mean value and error bar for a given quantity at one axial height; the mean values and error bars are then averaged over one pair of Taylor vortices. Apparently, for u_θ near the inner cylinder, both $\langle u_\theta \rangle_{t,z}$ and $\sigma(u'_\theta)$ decrease with volume fraction. The percentage of decrease for $\sigma(u'_\theta)$ can even reach up to approximately 20 %, indicating a strong suppression of the turbulence intensity near the inner cylinder with the presence of droplets.

To provide further insight, we analyse the PDFs of u_θ at $Re = 1.68 \times 10^4$ for different volume fractions ϕ, as depicted in figure 4(*a*). While the left-hand tails can be fitted with a Gaussian distribution (see the dashed line in figure 4*a*), the right-hand tails are

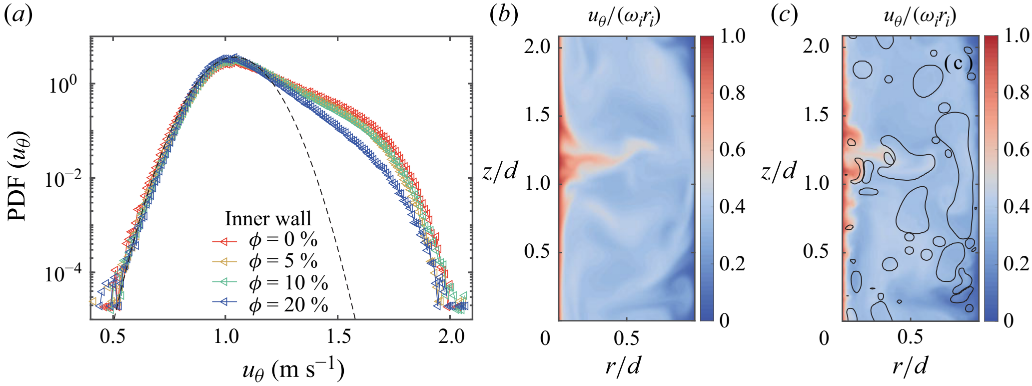

Figure 4. (*a*) The PDFs of the azimuthal velocity u_θ near the inner cylinder for varying volume fractions ϕ at $Re = 1.68 \times 10^4$. The black dashed line represents the Gaussian distribution fitted to the left-hand part of the data. The contour plots of the instantaneous azimuthal velocity field u_θ for the single-phase case (*b*) and the two-phase case with $\phi = 20\,\%$ (*c*) at $Re = 0.52 \times 10^4$. The solid lines in (*c*) indicate the interfaces of the droplets. Results in (*b*) and (*c*) are from the numerical simulation (Su *et al.* 2024*b*).

non-Gaussian. The overall PDFs are positively skewed. With the presence of droplets, the right-hand tails shrink as the volume fraction increases. In Rayleigh–Bénard (RB) turbulence, a nearly identical shape has been reported for the temperature PDF (Emran & Schumacher 2008). This PDF is induced by a combination of bursting plumes detaching from the thermal boundary layer and large-scale rolls (Castaing *et al.* 1989; Yakhot 1989; Procaccia *et al.* 1991). By using the TC–RB analogy (Eckhardt *et al.* 2007*a*), the skewness of the PDFs is similarly induced by plumes of angular velocity, with higher speeds dominating near the inner cylinder where herringbone-like patterns of streaks can form (Dong 2007; Froitzheim *et al.* 2019). The left- and right-hand tails of the PDFs are associated with low-speed and high-speed fluid, respectively. The high-speed fluid experiences greater centrifugal force that cannot be balanced by the pressure gradient in the radial direction. Consequently, it will be ejected from the velocity boundary layer, and this fluid is referred to as a plume. Therefore, the shrinkage of the right-hand tails with the increase in the volume fraction ϕ may indicate the suppression of angular velocity plumes.

To verify our conjecture, we show the contours of the azimuthal velocity from our numerical simulation in figure 4. The simulation details of the turbulent emulsion in TC flow can be found in our previous studies (Su *et al.* 2024*a*,*b*). For the two-phase case with $\phi = 20\,\%$, we also plot the interfaces of the droplets, shown as solid lines in figure 4(*c*). In the single-phase case (figure 4*b*), the plumes prefer to eject from the outflow region due to the presence of the Taylor vortex (Dong 2007). In the two-phase case (figure 4*c*), the droplet interface acts as a wall, preventing the plumes from penetrating through the interface. In this way, droplets block the ejection of plumes from the inner cylinder. This process results in the shrinkage of the PDFs in their right-hand tails. As a result, both the mean velocity and r.m.s. velocity fluctuation are reduced, as shown in figure 3(*b,c*).

When considering the global torque, it is directly related to the angular velocity flux J_ω, which is conserved in the radial direction, by the relation $J_\omega = G\nu_c^2$ (Eckhardt *et al.* 2007*a*,*b*). Here J_ω is defined as

$$J_\omega = J_{\omega,adv} + J_{\omega,dif} + J_{\omega,int}, \tag{3.1}$$

where the three terms represent (Hori *et al.* 2023):

(i) the advective contribution $J_{\omega,adv} = r^3\langle u_r\omega\rangle_{t,z}$ where $\omega = u_\theta/r$ is the angular velocity;
(ii) the diffusive contribution $J_{\omega,dif} = -r^3\nu\partial_r\langle\omega\rangle_{t,z}$;
(iii) the interfacial contribution $J_{\omega,int}$.

The interfacial contribution cannot be measured in experiment and we refer to our recent work (Su *et al.* 2025) for more details. For single-phase laminar flow, the first and third term vanishes due to $u_r = 0$, so only the second term contributes (Eckhardt *et al.* 2007*b*):

$$J_{\omega,lam} = 2\nu r_i^2 r_o^2\omega_i/(r_o^2 - r_i^2). \tag{3.2}$$

For two-phase flow, near the cylinder surface, the diffusive term plays a dominant role due to the no-slip condition and high angular velocity gradient. Consequently, the first term $J_{\omega,adv}$ in (3.1) can be neglected, and the second term $J_{\omega,dif}$ will dominate near the inner cylinder (Wang, DeGroot & Floryan 2023; Su *et al.* 2024*a*,*b*). The decrease of the mean azimuthal velocity $\langle u_\theta\rangle_{t,z}$ in figure 3(*b*) implies that the magnitude of the wall-normal velocity gradient $\partial_r\langle\omega\rangle_{t,z}$ will be augmented for a fixed $\tilde{r}$. Therefore, the angular velocity flux J_ω as well as the global torque G are enhanced.

3.2. *Modulation of continuous phase at the middle gap*

We then investigate the turbulence statistics at the middle gap, where both the azimuthal velocity u_θ and radial velocity u_r are measured (see figure 5*a*). The r.m.s. velocity fluctuations $\sigma(u'_\theta)$ and $\sigma(u'_r)$ are shown in figure 5(*b,c*). The velocity fluctuations decrease with the increase in volume fraction. Note that the small peak in figure 5(*c*) at $\phi = 5\,\%$ is within the error bar of our experimental measurement because u_r is much smaller than u_θ and therefore has a large uncertainty. In the bulk region of TC turbulence, the flow is close to homogeneous and isotropic turbulence (Grossmann *et al.* 2016). The suppression of velocity fluctuations by dispersed droplets has also been observed in numerical simulations of homogeneous and isotropic turbulence (Dodd & Ferrante 2016; Mukherjee *et al.* 2019; Crialesi-Esposito *et al.* 2022), where the suppression effect is attributed to the breakup of droplets by the large-scale turbulent fluctuations. During the breakup process, the TKE is transferred to the interfacial energy stored by the droplets.

At first glance, our results seem to be consistent with the numerical simulations of homogeneous and isotropic turbulence (Dodd & Ferrante 2016; Mukherjee *et al.* 2019; Crialesi-Esposito *et al.* 2022). However, this breakup mechanism cannot be applied to the middle gap of the TC turbulence. In our previous study, we found that the droplets cannot be fragmented by the turbulence fluctuations in the bulk region (Yi *et al.* 2022). To provide further evidence for this conjecture, we estimate the local Weber number using the measured velocity information. The local Weber number is defined as

$$We = \frac{\rho_c\langle\delta u_D^2\rangle_{t,z}\langle D\rangle}{\gamma}, \tag{3.3}$$

where $\langle\delta u_D^2\rangle_{t,z}$ is the average squared velocity increment over a distance equal to the droplet mean diameter $\langle D\rangle$ (Risso & Fabre 1998). In our experiment, $\langle\delta u_D^2\rangle_{t,z}$ can be estimated as follows:

$$\langle\delta u_D^2\rangle_{t,z} = \langle\delta u_\theta^2(\tau = \langle D\rangle/\langle u_\theta\rangle_{t,z})\rangle_{t,z}, \tag{3.4}$$

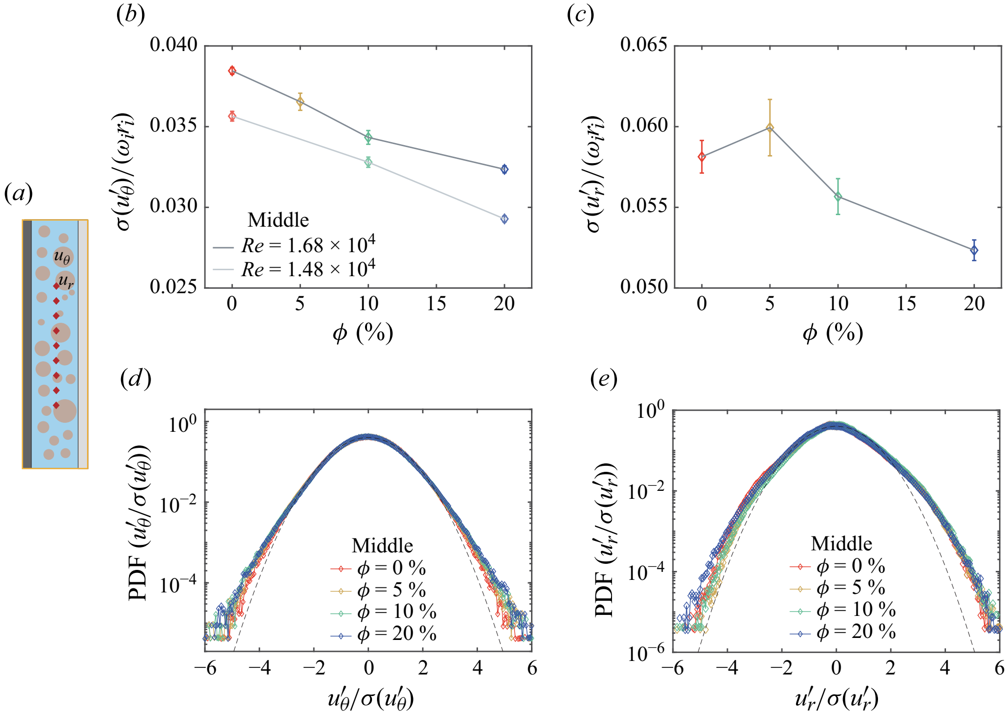

Figure 5. (*a*) A schematic shows the LDA measurement position at the midgap, represented by the red diamonds. Both azimuthal velocity u_θ and radial velocity u_r can be measured here. The r.m.s. velocity fluctuations for the azimuthal (*b*) and radial (*c*) velocities are shown with varying volume fraction ϕ for two different Reynolds numbers. The PDFs of the normalised azimuthal (*d*) and radial (*e*) velocities are also presented. The grey dashed lines correspond to the standard normal distribution.

where $\delta u_\theta(\tau) = u_\theta(t+\tau) - u_\theta(t)$ is the velocity increment over a time interval τ, and $\tau = \langle D \rangle / \langle u_\theta \rangle_{t,z}$ is the average time interval corresponding to the mean droplet diameter. Here we have invoked the Taylor frozen hypothesis since the turbulence fluctuation is much smaller than the mean velocity (Huisman *et al.* 2013*a*). Besides, $\langle \delta u_D^2 \rangle_{t,z}$ is calculated from the single-phase case, considering that the droplet size is measured at a volume fraction of $\phi = 1\,\%$. The value of local Weber number We at the middle gap is $We_{\tilde{r}=0.5} \approx 0.17 < 1$, suggesting that the turbulent fluctuation is not strong enough to break up the droplets in the bulk region (Yi *et al.* 2022). At higher volume fractions, the Weber number is $We_{\tilde{r}=0.5} \approx 0.14$, 0.12 and 0.11 at $\phi = 5\,\%$, $10\,\%$ and $20\,\%$, respectively, based on the same mean droplet diameter. Thus, the suppression of fluctuation in the bulk cannot be attributed to breakup-induced energy transfer. The suppression of the velocity fluctuation in the bulk can be understood as follows. The frequent burst of plumes also transfers energy from the inner cylinder to the bulk region. Since droplet interfaces block the emission of velocity plumes, less energy is injected into the bulk region resulting in lower turbulent fluctuations in both the azimuthal and radial directions.

We also include the PDFs of $u_\theta'/\sigma(u_\theta')$ and $u_r'/\sigma(u_r')$ in figure 5(*d,e*). Here u_θ' and u_r' are normalised by their r.m.s. velocity fluctuation. All PDFs are close to Gaussian distribution represented by the dashed lines, in line with previous study (Froitzheim *et al.* 2019). After normalisation, the PDFs collapse in their middle part. However, the tails of PDFs tend to become fatter as the volume fraction ϕ increases, indicating that turbulent emulsions are more intermittent than single-phase ones at large scales, i.e. the

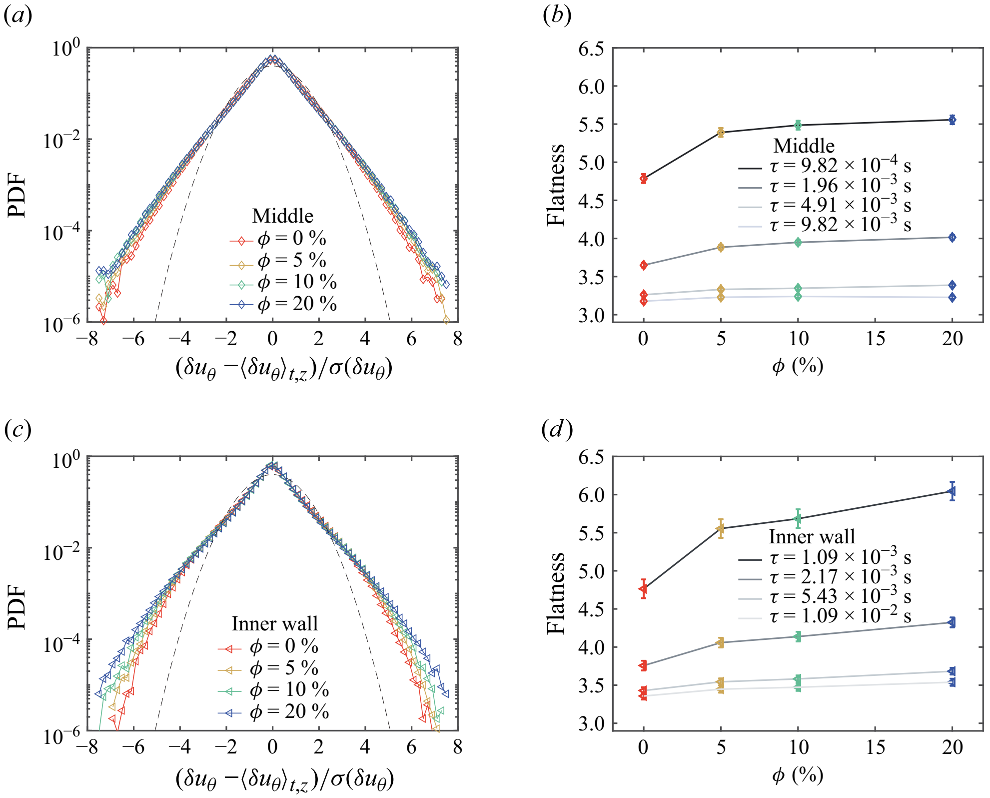

Figure 6. The PDFs of the velocity increment of azimuthal velocity component normalised by its mean and standard deviation at the middle gap (*a*) and near the inner cylinder (*c*). Here, the time interval $\tau = 9.82 \times 10^{-4}$ s in (*a*) and $\tau = 1.09 \times 10^{-3}$ s in (*c*). The grey dashed lines refer to the standard normal distribution. Flatness of velocity increment for several typical values of time interval with varying volume fraction at the middle gap (*b*) and near the inner cylinder (*d*).

intermittency of velocity fluctuation is enhanced. This behaviour has also been reported in droplet-laden homogeneous isotropic turbulence (Crialesi-Esposito *et al.* 2022). The enhanced intermittency in the bulk region at large scales originates from the presence of droplets. When the droplets deform and bounce back to the original spherical shape, the continuous phase adjacent to the droplets will experience extreme events due to the interfacial tension. This results in the intermittency enhancement at large scales at the middle gap.

Small-scale intermittency can be probed using the velocity increment $\delta u_\theta(\tau)$. The normalised PDFs of δu_θ, scaled by their mean and standard deviation, are plotted in figure 6(*a*) for the smallest time interval, $\tau = 9.82 \times 10^{-4}$ s, obtained in our experiment. The PDFs of δu_θ for a small τ are non-Gaussian, indicating small-scale intermittency. As the volume fraction increases, the tails of the PDFs become heavier than those in the single-phase case. To quantify this, we calculate the flatness of $\delta u_\theta(\tau)$ and $\langle \delta u_\theta^4(\tau) \rangle_{t,z} / \langle \delta u_\theta^2(\tau) \rangle_{t,z}^2$, for several values of τ, shown in figure 6(*b*). Taking the gap width d as the integral length scale and the azimuthal velocity of inner cylinder as the characteristic velocity, the corresponding integral time scale $t_i = d/r_i\omega_i \approx 4.7 \times 10^{-3}$ s, at which the level of intermittency should be similar to what we reported in figure 5(*d,e*). In general, the flatness of $\delta u_\theta(\tau)$ increases with the volume fraction of the dispersed phase for τ ranging from the smallest value measured in our experiment to the twice integral time scale. Similarly, we present the PDFs of the normalised δu_θ and their flatness for data measured near the inner cylinder in figure 6(*c,d*). Near the inner cylinder, the change in the PDF tails becomes more pronounced compared with the bulk region. The flatness also increases monotonically with the volume fraction. These results indicate that intermittency across the entire range of scales resolved here is enhanced in both the near-wall and bulk regions. We also note that the enhancement of intermittency is stronger in the near-wall region than in the bulk.

Intermittency in multiphase turbulence has attracted growing interest in recent years, driven by advancements in numerical simulations. Crialesi-Esposito *et al.* (2022, 2023*a*) investigated the PDFs of velocity and velocity increments, δu, between points conditioned to be located in the same phase or different phases. They found that the leading contribution to the increased deviation from Gaussian statistics at small scales comes from velocity increments across phase interfaces. However, the PDFs of $\delta u/\sigma(\delta u)_{SP}$, conditioned on points belonging to the continuous phase, remained nearly unchanged, where $\sigma(\delta u)_{SP}$ is the standard deviation of δu in the single-phase case. In our study, we use $\sigma(\delta u_\theta)$ from each respective case to normalise the velocity increment, as the flatness measures deviations from $\sigma(\delta u_\theta)$, not $\sigma(\delta u_\theta)_{SP}$. Crialesi-Esposito *et al.* (2024) further showed that the breakup of large droplets and the rupture of ligaments generate high vorticity and strain, which increases small-scale intermittency.

In light of these findings in homogeneous isotropic turbulence, we can interpret our results in TC turbulence. In the bulk region where the flow is nearly homogeneous and isotropic, the turbulence fluctuation is not strong enough to break up the droplets, as we have previously shown. The increased intermittency originates from the presence of interfaces as found by (Crialesi-Esposito *et al.* 2023*a*). Near the inner cylinder, droplets can be fragmented by the higher levels of shear, i.e. the dynamic pressure induced by the large mean velocity gradient (Levich 1962; Yi *et al.* 2022). We also note that the velocity plumes are able to deform large droplets, as shown in figure 4(*c*). During this process, the plume loses its energy in favour of the interface deformation. The large droplet deformation should then lead to the formation of several small scale structures, hence being responsible for the increase of intermittency. Therefore, the intermittency enhancement near the inner cylinder originates from not only the presence of interfaces but also the fragmentation and deformation of droplets. Consequently, additional intermittency beyond the presence of interfaces can be observed near the inner cylinder.

As we mentioned before, the global torque is directly related to angular velocity flux J_ω defined in (3.1). At the middle gap, the second term could be neglected due to the fact that the angular velocity gradient is small throughout the bulk region (Dong 2007; Froitzheim *et al.* 2019; Su *et al.* 2024*b*). In TC flow, the turbulence is a combination of turbulent Taylor vortices and background fluctuations. Thus, the first term $J_{\omega,adv} = r^3\langle u_r\omega\rangle_{t,z}$ can be further decomposed into two parts (Brauckmann & Eckhardt 2013):

$$r^3\langle u_r\omega\rangle_{t,z} = r^3\langle\langle u_r\rangle_t\langle\omega\rangle_t\rangle_z + r^3\langle u_r'\omega'\rangle_{t,z}. \tag{3.5}$$

These two terms are contributed by mean Taylor vortices and the turbulent fluctuation motion and can be denoted by their dimensionless forms, $Nu^M = r^3\langle\langle u_r\rangle_t\langle\omega\rangle_t\rangle_z/J_{\omega,lam}$ and $Nu^T = r^3\langle u_r'\omega'\rangle_{t,z}/J_{\omega,lam} = r^2\langle u_\theta' u_r'\rangle_{t,z}/J_{\omega,lam}$, respectively.

We first study the effect of droplets on the Taylor vortices. We plot in figure 7(*a*) the axial profiles of the radial velocity for different volume fractions from $\phi = 0\,\%$ to $\phi = 20\,\%$ at $Re = 1.68 \times 10^4$ and the average azimuthal velocity with varying ϕ at two different Re in figure 7(*b*). These u_r profiles approximately overlap with each other. For $\langle u_\theta\rangle_{t,z}$, it also remains nearly unchanged at various ϕ explored in our experiment, implying that

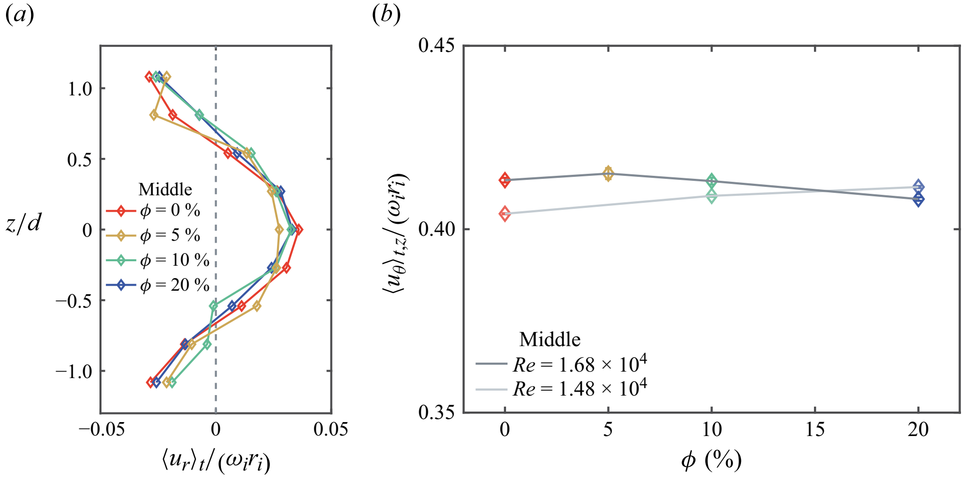

Figure 7. (*a*) Axial profiles of the mean radial velocity, normalised by the inner cylinder velocity, $\langle u_r \rangle_t/(\omega_i r_i)$, for different volume fractions from $\phi = 0\,\%$ to $\phi = 20\,\%$ at $Re = 1.68 \times 10^4$. (*b*) Mean azimuthal velocity, normalised by the inner cylinder velocity, $\langle u_\theta \rangle_{t,z}/(\omega_i r_i)$, with varying volume fraction ϕ for two Reynolds numbers.

the existence of droplets would not change the mean flow dramatically, at least in the present parameter range. In all, the angular velocity flux and global torque contributed by the Taylor vortices in the bulk region remain almost unchanged as the droplets have a marginal effect on them.

We then explore the turbulence contribution to the angular velocity flux and plot PDFs of dimensionless angular velocity flux $r^2 u'_\theta u'_r / J_{\omega,lam}$ in figure 8(*a*). Note that when calculating the production of u'_θ and u'_r, the series of velocity component with higher data rate is interpolated based on the other one with lower data rate. The PDFs are all positively skewed since the momentum has to be transported to the outer cylinder, which is consistent with previous studies (Huisman *et al.* 2012*a*; Brauckmann & Eckhardt 2013; Froitzheim *et al.* 2019). Furthermore, they are highly non-Gaussian, which is reflected by the observation that the local flux $r^2 u'_\theta u'_r$ taking values ±400 times as large as $J_{\omega,lam}$ still has a high probability of occurrence (Huisman *et al.* 2012*a*; Froitzheim *et al.* 2019). These large rare events are found to be footprints of angular velocity flux fluctuations induced by plumes, similar behaviours are also reported in RB turbulence (Shang *et al.* 2003). With the presence of droplets, both tails of the PDFs shrink as ϕ increases, implying that the large rare events are suppressed. The reduced probability of rare angular velocity flux events is an additional sign that the droplet interfaces can block the emission of angular velocity plumes near the inner cylinder, providing further evidence to our conclusion made in § 3.1. We also note that these large rare events make the measurement of Nu^T quite challenging as already reported in Huisman *et al.* (2012*a*) and Froitzheim, Merbold & Egbers (2017), which results in uncertainty in Nu^T.

Since the droplets inhibit the turbulent fluctuations of both the azimuthal and radial velocity (the percentage of depression is up to 15 % for $\sigma(u'_\theta)$ at $\phi = 20\,\%$), we would expect that the angular velocity flux contributed from the turbulence would be suppressed accordingly, i.e. the overall profiles of PDFs for two-phase cases would be shifted horizontally. However, the decreasing tendency of Nu^T is not observed in our experiment. Instead, Nu^T fluctuates around a constant within the experimental uncertainties (see the inset of figure 8*a*). Thus, the angular velocity flux and global torque contributed by the turbulent flow in the bulk region also remain almost unchanged.

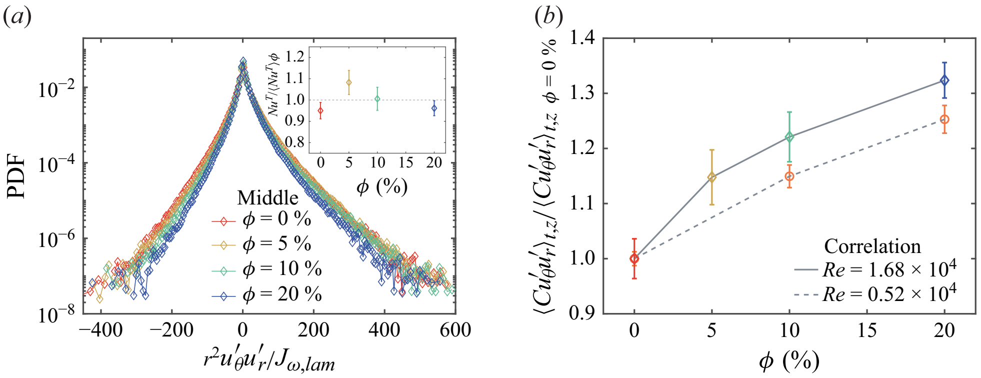

Figure 8. (*a*) The PDFs of dimensionless angular velocity flux normalised by the corresponding laminar angular velocity flux, i.e. $r^2u'_\theta u'_r/(J_{\omega,lam})$. Inset: average angular velocity flux contributed by the turbulent flow Nu^T normalised by $\langle Nu^T\rangle_\phi$, which is the average Nusselt number over all volume fractions. Data are from $Re = 1.68 \times 10^4$. (*b*) The cross-correlation coefficients between u'_θ and u'_r as a function of volume fraction normalised by the single-phase case at $Re = 1.68 \times 10^4$ (diamond mark) measured in our experiment and at $Re = 0.52 \times 10^4$ obtained from the numerical simulation (circle mark) (Su *et al.* 2024*a*).

Taken together, we show that the advective contributions to global torque by the mean flow and turbulence fluctuations remain nearly unmodified in the bulk region. We therefore conclude that the drag enhancement presumably originates from the effect of two-phase interfaces, which cannot be quantified in the experiment but has already been investigated in our previous simulation work (Su *et al.* 2024*a*,*b*).

From the inset of figure 8(*a*), we found that $Nu^T/\langle Nu^T\rangle_\phi$ fluctuates around 1, and does not show a ϕ dependence. To investigate the reason of nearly constant Nu^T, we make a further conversion of the second term in (3.5),

$$r^3\langle u'_r\omega'\rangle_{t,z} = r^2\langle u'_r u'_\theta\rangle_{t,z} = r^2\sigma(u'_\theta)\sigma(u'_r)\langle C_{u'_\theta u'_r}\rangle_{t,z}, \tag{3.6}$$

where $\langle C_{u'_\theta u'_r}\rangle_{t,z}$ refers to the cross-correlation coefficient between the azimuthal and radial velocity, which is defined as

$$\langle C_{u'_\theta u'_r}\rangle_{t,z} = \frac{\langle u'_\theta u'_r\rangle_{t,z}}{\sigma(u'_\theta)\sigma(u'_r)}. \tag{3.7}$$

The concept of cross-correlation has been widely adopted in the single-phase TC turbulence (Burin, Schartman & Ji 2010; Brauckmann, Salewski & Eckhardt 2016; Huisman *et al.* 2012*a*). Equation (3.6) indicates that only the correlated fluctuations of u'_θ and u'_r contribute to the net convective transportation. Therefore, the cross-correlation coefficient is calculated for varying ϕ and averaged over different heights, being illustrated in figure 8(*b*), where we also include the results from our numerical simulation. For the two-phase case, $\langle C_{u'_\theta u'_r}\rangle_{t,z}$ exhibits clear and monotonic enhancement behaviours with the increase of ϕ. The enhancement of $\langle C_{u'_\theta u'_r}\rangle_{t,z}$ is more than 30 % at $\phi = 20$ %, indicating that the turbulent emulsion becomes more coherent than the single-phase flow due to the presence of droplets. Here $\langle C_{u'_\theta u'_r}\rangle_{t,z}$ from the numerical simulation also displays an enhancement but to a lesser degree, which may be related to the different Reynolds number in the experiments and numerical simulation. Thus, the nearly constant of Nu^T can be attributed to the enhanced coherence. Since the turbulence becomes more intermittent as discussed above and the breakup and coalescence events of droplets are found to create disturbances on coherent structures (Dodd & Ferrante 2016; Perlekar 2019;

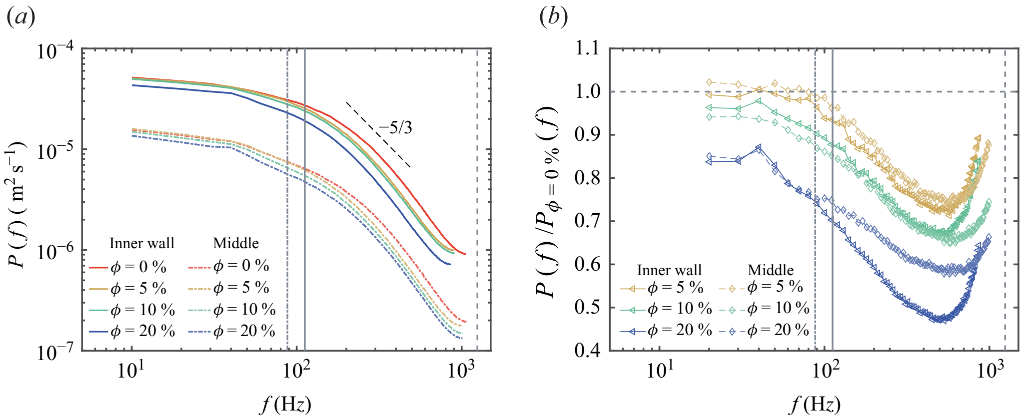

Figure 9. (*a*) Velocity power spectra $P(f)$ for the azimuthal velocity u'_θ near the inner cylinder (solid line) and at the middle gap (dash–dotted line). The thin dashed line with a slope of $-5/3$ represents the inertial range scaling exponent at high Reynolds numbers. (*b*) Here $P(f)$ for the two-phase cases is scaled by its single-phase counterpart, i.e. $P(f)/P_{\phi=0\,\%}(f)$. The vertical grey solid and dash–dotted lines refer to the characteristic frequencies corresponding to the gap width, $\langle u_\theta \rangle_{t,z}/d$, near the inner cylinder and at the middle gap, respectively. The vertical grey dashed line denotes the frequency, $\langle u_\theta \rangle_{t,z}/\langle D \rangle$, corresponding to the mean droplet diameter at the middle gap, where we conduct the droplet size measurement. Data are from $Re = 1.68 \times 10^4$.

Crialesi-Esposito *et al.* 2022), we are surprised to observe that the turbulence coherence is enhanced by the dispersed droplets. In the case of turbulent emulsion, the continuous phase is surrounded by dispersed droplets. The continuous phase fluid thus cannot evolve freely like it could do in the single-phase case due to the confinement of the surrounding droplets. This conjecture needs to be tested in future studies.

3.3. *Velocity power spectrum*

As we have discussed, the turbulence fluctuation is suppressed by the presence of droplets near the inner cylinder and at the middle gap. It is known that turbulence implies fluid motion across a wide spectrum of length and time scales (Pope 2000). Thus, it is also instructive to investigate the effect of droplets on the multiscale nature of turbulence. This can be accomplished by inspecting the velocity power spectra of the azimuthal velocity fluctuation u'_θ. Because the arrival times of LDA measurements are stochastic in nature, the time series are then linearly interpolated using twice the average acquisition frequency (Huisman *et al.* 2013*a*), aiming to create a time series with equal temporal spacing, which facilitates the application of fast Fourier transformation. The power spectra near the inner cylinder, as well as at the middle gap for different volume fractions, are shown in figure 9(*a*). We also illustrate two characteristic frequencies, namely the frequency corresponding to the gap width $\langle u_\theta \rangle_{t,z}/d$ near the inner cylinder (vertical solid line) and at the middle gap (dashed–dotted line), and the frequency corresponding to the mean droplet diameter $\langle u_\theta \rangle_{t,z}/\langle D \rangle$ (vertical dashed line). Due to measurement limitations, frequencies higher than $\langle u_\theta \rangle_{t,z}/\langle D \rangle$ cannot be resolved in this study. The inertial range scaling is expected to appear in the range of frequencies $f > \langle u_\theta \rangle_{t,z}/d$. In the bulk, we also use the Taylor scale-based Reynolds number to measure turbulence intensity, which is defined as

$$R_\lambda = \frac{\sigma(u'_\theta)\lambda}{\nu_c} = \sqrt{\frac{15\sigma(u'_\theta)^4 \epsilon}{\nu_c}}, \tag{3.8}$$

where the average energy dissipation rate ϵ is estimated by the global torque $\epsilon = 0.1T\omega_i/(\pi(r_o^2 - r_i^2)L\rho_c)$ (Ezeta *et al.* 2018; Yi *et al.* 2022). At $Re = 1.68 \times 10^4$, $R_\lambda \approx 70$. The R_λ is too low to observe a clear inertial range scaling. Nevertheless, we show the $-5/3$ scaling (thin dashed line) in figure 9(*a*) as a reference.

Firstly, the amplitude of the velocity power spectra obtained near the inner cylinder is much higher than that at the middle gap, indicating that the turbulence near the inner cylinder is substantially stronger than at the middle gap. This finding was also captured by Dong (2007), which shows an uneven distribution and asymmetry in the intensity of turbulent fluctuations caused by the curvature effect. When comparing the single-phase and two-phase cases near the inner cylinder, it seems that at very large scales the kinetic energy increases for the $\phi = 5\,\%$ case. However, the deviation of the $\phi = 5\,\%$ case from 1 is less than 3 % which could be seen from figure 9(*b*). This deviation is small and within the experimental uncertainty. Therefore, it can be concluded that the energy content of turbulent fluctuations at all scales resolved in our experiment is strongly depressed, especially at scales smaller than d, i.e. frequencies higher than $\langle u_\theta \rangle_{t,z}/d$. This result is consistent with previous simulation works (Perlekar *et al.* 2014; Dodd & Ferrante 2016; Mukherjee *et al.* 2019; Rosti *et al.* 2019; Crialesi-Esposito *et al.* 2022, 2023*a*; Trefftz-Posada & Ferrante 2023). Even though these simulations studied different kinds of turbulent flows, such as homogeneous isotropic turbulence (Perlekar *et al.* 2014; Dodd & Ferrante 2016; Mukherjee *et al.* 2019; Crialesi-Esposito *et al.* 2022, 2023*b*) and homogeneous shear turbulence (Rosti *et al.* 2019; Trefftz-Posada & Ferrante 2023), energy spectrum suppression at scales larger than the average droplet diameter is consistently observed. Moreover, as the number of droplets increases, the degree of suppression on turbulence fluctuations also rises.

Regarding the mechanism, one widely accepted hypothesis is as follows: in Newtonian turbulence, the nonlinear energy flux of the fluid is the only energy transfer mechanism. In turbulent emulsions, droplets provide an additional mechanism of energy transfer due to the frequent breakup and deformation of the droplets; the TKE can be transferred from the fluid to the interfacial energy stored by the droplets (Perlekar 2019; Crialesi-Esposito *et al.* 2022). The higher the volume fraction, the greater the likelihood of deformation and breakup events, resulting in a higher degree of suppression of TKE at scales larger than the mean droplet size. This hypothesis offers a reasonable explanation for the energy spectrum suppression near the inner cylinder, while at the middle gap, the suppression results from reduced ejection of plumes near the inner cylinder, leading to less energy being transported into the bulk region. The simulation results also indicate that the spectrum at scales smaller than the mean droplet diameter is greatly enhanced, presumably due to the coalescence of small droplets, which feeds the interfacial energy back into the fluid. The increased energy content at scales smaller than the mean droplet diameter needs to be verified in future studies.

To compare the effects of droplets on the spectrum near the inner cylinder and at the middle gap, the spectrum of the two-phase case is scaled by its single-phase counterpart, i.e. $P(f)/P_{\phi=0\,\%}(f)$, as shown in figure 9(*b*). It is clear that the suppression effect becomes stronger as the frequency increases (or the scale decreases). The faster decay of $P(f)$ when $f > \langle u_\theta \rangle_{t,z}/d$ suggests that the scaling of the spectrum is modified, as also reported in Perlekar *et al.* (2014). We note that the roll-up of $P(f)/P_{\phi=0\,\%}(f)$ at high frequency is due to instrument noise (Huisman *et al.* 2013*a*), which is also reflected in the levelling-off of $P(f)$ in figure 9(*a*).

At low volume fractions ($\phi = 5\,\%$ and 10 %), the $P(f)/P_{\phi=0\,\%}(f)$ curves nearly collapse near the inner cylinder and at the middle gap, indicating that the suppression effect is similar at these two positions. At a higher volume fraction ($\phi = 20\,\%$), the suppression effect is stronger near the inner cylinder than at the middle gap for frequencies higher than $\langle u_\theta \rangle_{t,z}/d$ (scales smaller than the gap width d). One possible explanation is that, at high volume fractions, the droplets have a higher probability of merging with each other, which in turn releases the interfacial energy back to the fluid at the middle gap since the droplets are less likely to break apart there.

4. Conclusion

In this work, we experimentally investigate how the dispersed droplets modulate the global drag and the statistical properties of turbulence velocity fluctuations in the continuous phase of a turbulent emulsion. The emulsion is generated in a turbulent TC flow. We precisely match the refractive indices of the dispersed and continuous phases, which facilitates our measurement of the local velocity of the continuous phase for volume fractions of up to $20\,\%$. Due to the inhomogeneity of the TC flow, the velocity measurements are performed at two representative radial locations: near the inner cylinder and at the middle gap.

Near the inner cylinder, the droplet interfaces can suppress the emission of angular velocity plumes from the boundary layer, resulting in a reduction in both the mean azimuthal velocity and the r.m.s. fluctuation of azimuthal velocity. This reduction in the mean azimuthal velocity leads to a higher gradient of angular velocity in the radial direction, thus increasing the viscous diffusion contribution to the angular velocity flux and global drag of the system. By comparing the velocity power spectrum, we find that the energy content at scales above the average droplet diameter is depressed, which results from the reduced emission of plumes and breakup-induced energy transfer from the fluid to the interfacial energy of the droplets.

At the middle gap, the angular velocity flux contributed by the mean Taylor vortex, Nu^M, and the turbulence, Nu^T, are nearly unaltered by the droplets. The droplets enhance the cross-correlation between the angular and radial velocity, which compensates for the reduction in velocity fluctuation, leaving Nu^T unchanged. However, the rare events of angular velocity flux contributed by the turbulent flow are less frequent due to the reduced plume emission. We further show that the intermittency of velocity increments is enhanced due to the presence of interfaces. A similar behaviour is observed near the inner cylinder, but the degree of enhancement is higher at small scales, which may be related to the breakup-induced generation of high vorticity and strain.

In this study, we present the first attempt to gather velocity information in a wall-bounded turbulent emulsion. Our study provides valuable experimental insights into how the dispersed droplets modulate global drag, coherent structures and the multiscale nature of the turbulent flow. In future work, we aim to further improve the measurement techniques to simultaneously capture the velocities of both the continuous and dispersed phases in dense turbulent emulsions, studying the detailed coupling dynamics of the two phases.

Acknowledgements. We acknowledge Y. Liu for insightful discussions on the experimental methods. We thank F. Toschi, X.M. de Wit and S. Huisman for their insightful discussions and suggestions.

Funding. This work is financially supported by the National Natural Science Foundation of China under grant nos. 11988102, 12402298 and 12402299, the New Cornerstone Science Foundation through the New Cornerstone Investigator Program and the XPLORER PRIZE.

Declaration of interests. The authors report no conflict of interest.

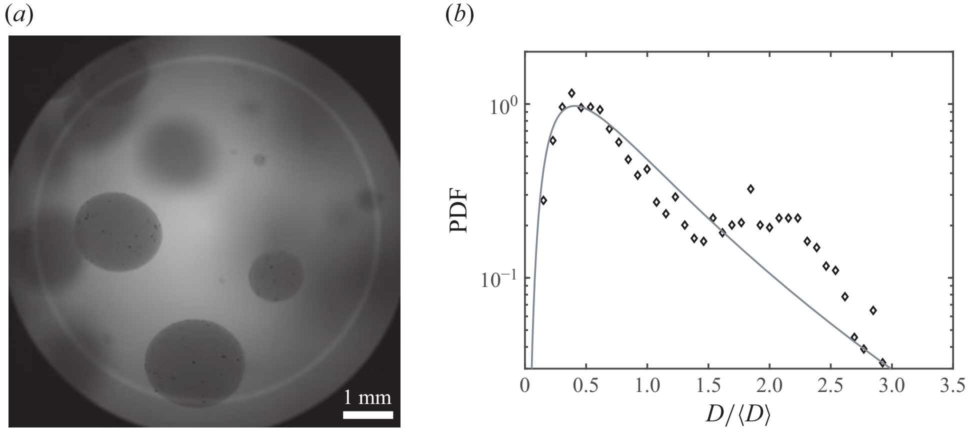

Figure 10. (*a*) Typical snapshot of the droplets at $\phi = 1\ \%$ recorded with a high-speed camera connected with a long-distance microscope. (*b*) The PDF of the normalised droplet size at $\phi = 1\ \%$. The grey solid line represents the log-normal distribution (Yi *et al.* 2021).

Appendix A. The measurement of droplet size

The droplet size is measured at $Re = 1.68 \times 10^4$ with a volume fraction $\phi = 1\ \%$ in the bulk region of TC flow and the average droplet size is $\langle D\rangle \approx 700\ \mu\text{m}$. The typical snapshot of droplets and the droplet size distribution are shown in figures 10(*a*) and 10(*b*). We also show the log-normal distribution reported by Yi *et al.* (2021). Our experimental data is consistent with previous study. To obtain the droplet size distribution, one needs a large amount of data. At volume fraction of $\phi \geq 5\ \%$, the interfaces overlap with each other on the captured image, and it is difficult to collect enough data to yield a converged distribution. The detailed droplet size distribution may change at different volume fractions, and this remains an open question to be answered in future study. In this work, we use $\langle D\rangle \approx 700\ \mu\text{m}$ to represent the mean diameter size in the bulk region at all volume fractions from $\phi = 5\ \%$ to $\phi = 20\ \%$.

As reported in our previous study (Yi *et al.* 2022), the mean droplet diameter remains nearly constant when the volume fraction of dispersed phase is less than 50 %, which is related to the presence of unavoidable surface-active impurities in the solution suppressing droplet merging. In our previous work (Yi *et al.* 2022) and this study, we use the same flow configuration, and the density and viscosity between the continuous and dispersed phases are nearly matched. The only difference comes from the surface tension: $\gamma \approx 21.1$ and 5.5 mN m^{-1} in this study and previous work, respectively. The value of γ will not change the physical mechanism of droplet breakup and coalescence in TC turbulence. Therefore, it is reasonable to use $\langle D\rangle \approx 700\ \mu\text{m}$ to represent the average droplet size at higher volume fractions, which is $0\ \% - 20\ \%$ in this study.

Regarding the radial dependence of droplet size, the TC system can be divided into two parts: the boundary layer near the inner and outer cylinder, the bulk where the flow is nearly homogeneous and isotropic. We would expect smaller droplet size near the boundary layer due to the high shear of the mean velocity (Yi *et al.* 2022), and a nearly constant droplet size in the bulk. However, as the boundary layer thickness is small, it is difficult to measure the droplet size near the inner cylinder (Yi *et al.* 2021).

The radial distribution of droplet number has been investigated by Wang *et al.* (2022*a*,*b*). At low Reynolds number, there will be a clustering behaviour near the inner cylinder at

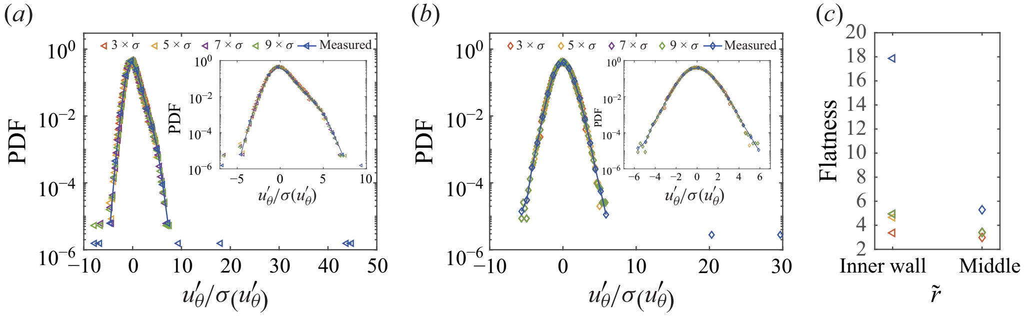

Figure 11. The PDFs of times series of u_θ (*a*) near the inner cylinder and (*b*) at the middle gap using several different thresholds of three, five, seven and nine times the r.m.s. (*c*) The corresponding flatness values for each cases. Inset: the zoom-in of the main part of the PDFs.

the region where the plumes of angular velocity are injected. However, at higher Reynolds number $Re = 1.3 \times 10^4$ which is still lower than the present study, the spatial distribution becomes nearly uniform in the bulk region due to the high turbulence fluctuation. For our case with higher Reynolds number ($Re = 1.48 \sim 1.68 \times 10^4$), we would expect that the droplets distribution over the radial direction is nearly uniform.

Appendix B. Data processing of velocity time series

Regarding the LDA data quality, noise, including stochastic noise from the photodetector and electronics as well as the reflection from the experimental set-up, cannot be avoided in the experiment. The following ways were tried to improve the data quality throughout the experiment procedure. First, we set a proper velocity range for each LDA signal channel by properly tuning the frequency shift of the Bragg cell. Second, the inner cylinder is anodised to form a black oxidation layer and the upper cover of the set-up is made of black acrylonitrile butadiene styrene. The black inner cylinder and upper cover can alleviate laser reflection from solid surface as mentioned in § 2.1. Third, for each LDA data series, we used seven times the r.m.s. value of raw data to filter out the outlier data. The amount of outlier data is less than 1 ‱.

The range of ±7 times the r.m.s. value was selected to eliminate outlier data without severely changing the shape of the PDF as well as the values of flatness. Taking u_θ at a certain height at $\phi = 20\,\%$ as an example, the PDFs and the values of flatness using several different thresholds of three, five, seven and nine times the r.m.s. are shown in figure 11. It reveals outliers (lower right) in the normalised velocity PDFs of u_θ throughout both the near-wall and middle regions, which are identified as non-physical artefacts requiring exclusion. The insets in figure 11(*a–b*) demonstrate the filtering performance at different r.m.s. multiplier thresholds: while thresholds of three and five induce artificial truncation of the PDFs tails, values of seven and nine exhibit excellent fidelity in preserving the intrinsic flow characteristics while effectively eliminating outlier contamination. Furthermore, flatness analysis reveals a saturation trend with increasing r.m.s. multipliers: the flatness values for seven and nine become statistically indistinguishable (evidenced by marker overlap in the plot). The discrepancy between raw and processed data flatness originates from the aforementioned invalid outliers. We therefore conclude that the choice of seven times the r.m.s. value provides the best cutoff without affecting the shape of PDF profiles. In our study, the 7σ threshold yields data exclusion rate smaller than 1 ‱. While a 1 ‱ exclusion rate would typically correspond to a 4σ cutoff in a standard Gaussian distribution, the velocity fluctuations in turbulent flows exhibit deviations from Gaussian statistics due to intermittency. This intermittency leads to elevated tails in PDFs, causing the higher rate of outlier data than a Gaussian distribution.

For LDA measurements, the spatial integration of signals due to the finite size of the measurement volume affects turbulence measurements particularly at the near-wall region (Durst, Jovanović & Sender 1995). Following their method, the estimations of the magnitude of corrections on $\langle u_\theta \rangle$ and $\sigma(u'_\theta)^2$ are shown below. We denote the relative correction to be

$$\Delta_{\langle u_\theta \rangle_{t,z}} / \langle u_\theta \rangle_{t,z} = \frac{d^2}{32} \left(\frac{\mathrm{d}^2 u_{\theta,true}}{\mathrm{d}y^2} \right) / \langle u_\theta \rangle_{t,z}, \tag{B1}$$

$$\Delta_{\sigma(u'_\theta)^2} / \sigma(u'_\theta)^2 = \frac{d^2}{16} \left(\frac{\mathrm{d}u_{\theta,true}}{\mathrm{d}y} \right)^2 / \sigma(u'_\theta)^2, \tag{B2}$$

if we take the first term of Taylor expansion (Durst *et al.* 1995). It can be found that the relative corrections depend only on streamwise velocity gradient at the measurement point.

In the single-phase case, the boundary layer velocity profile obtained by Zhang *et al.* is employed for estimation of the correction. Based on figure 13 in Zhang *et al.* (2025), the azimuthal velocity profiles in the log layer could be approximately described by $u_\theta^+ = 1/\kappa \ \ln y^+ + B$ at $Re = 1.68 \times 10^5$ and $y^+ = 35 \pm 9$, where $u_\theta^+ = (\omega_i r_i - \langle u_\theta \rangle_{t,z})/u_\tau = (\omega_i r_i - \langle u_\theta \rangle_{t,z})/\sqrt{T/(2\pi \rho_c r_i^2 L)}$, $y^+ = (r - r_i)/\delta_\nu$ and $\kappa \approx 1$ here (estimated from figure 13b in Zhang *et al.* (2025)). Therefore, $\mathrm{d}^2 u_{\theta,true}/\mathrm{d}y^2 = u_\tau / y^2$ and $(\mathrm{d}u_{\theta,true}/\mathrm{d}y)^2 = (u_\tau / y)^2$. Then we have

$$\Delta_{\langle u_\theta \rangle_{t,z}} / \langle u_\theta \rangle_{t,z} = \frac{d^2 u_\tau}{32 y^2 \langle u_\theta \rangle_{t,z}} \approx 6.75 \times 10^{-4}, \tag{B3}$$

$$\Delta_{\sigma(u'_\theta)^2} / \sigma(u'_\theta)^2 = \frac{d^2 u_\tau^2}{16 y^2 \sigma(u'_\theta)^2} \approx 4.79 \times 10^{-3}. \tag{B4}$$

We find that the correction to $\langle u_\theta \rangle_{t,z}$ is smaller than the correction to $\sigma(u'_\theta)^2$, and both corrections are less than 1 %. This small correction is consistent with previous study (Durst *et al.* 1995). Durst *et al.* (1995) reported that the correction is necessary in the viscous sublayer due to the large velocity gradient, while the correction in the log layer is negligible.

For the two-phase cases at different volume fraction, the mean streamwise velocity profile is not known *a priori*. Roccon *et al.* (2017) have done numerical simulations in wall-bounded turbulent emulsions with volume fraction $\phi = 18.6\,\%$. They found that the mean streamwise velocity of the two-phase flow shifts slightly upwards with its slope $(1/\kappa)$ in the log layer nearly unchanged. Therefore, we can still use (B3) and (B4) to calculate the relative corrections. For the two-phase case at the maximum volume fraction $(\phi = 20\,\%)$, $\Delta_{\sigma(u'_\theta)^2}/\sigma(u'_\theta)^2 \approx 7.37 \times 10^{-3}$, which is still less than 1 %. Consequently, these data acquired is reliable and the effects induced by the finite measurement volume can be considered negligible.

To investigate the effect of droplets on the measured LDA temporal signal, we calculate the PDFs of the time interval, Δ_t, between neighbour velocity data, which is shown in figure 12. The horizontal axis is scaled by the average time interval, i.e. $\langle \Delta_t \rangle$. We note that $\langle \Delta_t \rangle$ in the single-phase and two-phase cases are nearly the same and the average data rate is $1/\langle \Delta_t \rangle$. The vertical dashed line denotes the average passing time of one droplet $\langle D \rangle / \langle u_\theta \rangle_{t,z}$. In our experiment, $\langle \Delta_t \rangle > \langle D \rangle / \langle u_\theta \rangle_{t,z}$. It can be found that the PDFs are almost collapsed on the top of each other. Thus, the effect of droplets

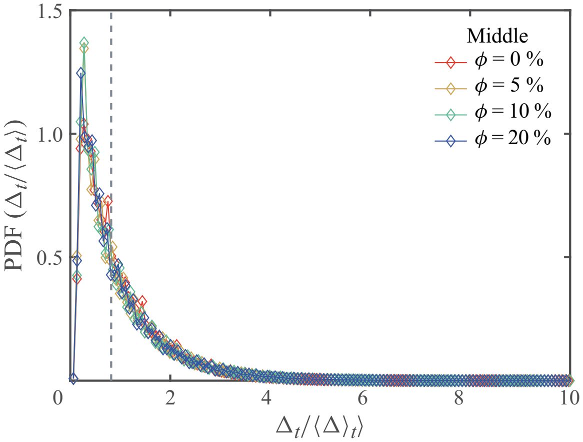

Figure 12. The PDFs of the time intervals between two neighbour velocity data points. Here, we use u_θ measured near the inner cylinder as an example. The vertical dashed line corresponds to the average droplet passing time, i.e. $\langle D\rangle/\langle u_\theta\rangle_{t,z}$.

on the measured temporal signal, if it is present, is only marginal for the current study. One possible explanation for this observation is that $\langle\Delta_t\rangle > \langle D\rangle/\langle u_\theta\rangle_{t,z}$ and the average spacing between neighbour droplets is larger than $\langle\Delta_t\rangle\langle u_\theta\rangle_{t,z}$ due to the 'low' volume fraction. We therefore conclude that the influence of droplets on time series of velocity is negligible.

REFERENCES

AMINI, N. & HASSAN, Y.A. 2012 An investigation of matched index of refraction technique and its application in optical measurements of fluid flow. *Exp. Fluids* **53** (6), 2011–2020.

BAKHUIS, D., EZETA, R., BULLEE, P.A., MARIN, A., LOHSE, D., SUN, C. & HUISMAN, S.G. 2021 Catastrophic phase inversion in high-Reynolds-number turbulent Taylor–Couette flow. *Phys. Rev. Lett.* **126** (6), 064501.

BEGEMANN, A., TRUMMLER, T., TRAUTNER, E., HASSLBERGER, J. & KLEIN, M. 2022 Effect of turbulence intensity and surface tension on the emulsification process and its stationary state—A numerical study. *Can. J. Chem. Engng* **100** (12), 3548–3561.

BRAUCKMANN, H.J. & ECKHARDT, B. 2013 Direct numerical simulations of local and global torque in Taylor–Couette flow up to Re = 30 000. *J. Fluid Mech.* **718**, 398–427.

BRAUCKMANN, H.J., SALEWSKI, M. & ECKHARDT, B. 2016 Momentum transport in Taylor–Couette flow with vanishing curvature. *J. Fluid Mech.* **790**, 419–452.

BUDWIG, R. 1994 Refractive index matching methods for liquid flow investigations. *Exp. Fluids* **17** (5), 350–355.

BURIN, M.J., SCHARTMAN, E. & JI, H. 2010 Local measurements of turbulent angular momentum transport in circular Couette flow. *Exp. Fluids* **48** (5), 763–769.

CASTAING, B., GUNARATNE, G., HESLOT, F., KADANOFF, L., LIBCHABER, A., THOMAE, S., WU, X.-Z., ZALESKI, S. & ZANETTI, G. 1989 Scaling of hard thermal turbulence in Rayleigh–Bénard convection. *J. Fluid Mech.* **204**, 1–30.

CONAN, C., MASBERNAT, O., DÉCARRE, S. & LINÉ, A. 2007 Local hydrodynamics in a dispersed-stratified liquid–liquid pipe flow. *AICHE J.* **53** (11), 2754–2768.

CRIALESI-ESPOSITO, M., BOFFETTA, G., BRANDT, L., CHIBBARO, S. & MUSACCHIO, S. 2023*a* Intermittency in turbulent emulsions. *J. Fluid Mech.* **972**, A37.

CRIALESI-ESPOSITO, M., CHIBBARO, S. & BRANDT, L. 2023*b* The interaction of droplet dynamics and turbulence cascade. *Commun. Phys.* **6** (1), 5.

CRIALESI-ESPOSITO, M., BOFFETTA, G., BRANDT, L., CHIBBARO, S. & MUSACCHIO, S. 2024 How small droplets form in turbulent multiphase flows. *Phys. Rev. Fluids* **9** (7), L072301.

CRIALESI-ESPOSITO, M., ROSTI, M.E., CHIBBARO, S. & BRANDT, L. 2022 Modulation of homogeneous and isotropic turbulence in emulsions. *J. Fluid Mech.* **940**, A19.

Dodd, M.S. & Ferrante, A. 2016 On the interaction of Taylor length scale size droplets and isotropic turbulence. *J. Fluid Mech.* **806**, 356–412.

Dong, S. 2007 Direct numerical simulation of turbulent Taylor–Couette flow. *J. Fluid Mech.* **587**, 373–393.

Durst, F., Jovanović, J. & Sender, J. 1995 LDA measurements in the near-wall region of a turbulent pipe flow. *J. Fluid Mech.* **295**, 305–335.

Eckhardt, B., Grossmann, S. & Lohse, D. 2007*a* Fluxes and energy dissipation in thermal convection and shear flows. *Europhys. Lett.* **78** (2), 24001.

Eckhardt, B., Grossmann, S. & Lohse, D. 2007*b* Torque scaling in turbulent Taylor–Couette flow between independently rotating cylinders. *J. Fluid Mech.* **581**, 221–250.

Emran, M.S. & Schumacher, J. 2008 Fine-scale statistics of temperature and its derivatives in convective turbulence. *J. Fluid Mech.* **611**, 13–34.

Eskin, D., Taylor, S.D. & Yang, D. 2017 Modeling of droplet dispersion in a turbulent Taylor–Couette flow. *Chem. Engng Sci.* **161**, 36–47.

Ezeta, R., Huisman, S.G., Sun, C. & Lohse, D. 2018 Turbulence strength in ultimate Taylor–Couette turbulence. *J. Fluid Mech.* **836**, 397–412.

Froitzheim, A., Ezeta, R., Huisman, S.G., Merbold, S., Sun, C., Lohse, D. & Egbers, C. 2019 Statistics, plumes and azimuthally travelling waves in ultimate Taylor–Couette turbulent vortices. *J. Fluid Mech.* **876**, 733–765.

Froitzheim, A., Merbold, S. & Egbers, C. 2017 Velocity profiles, flow structures and scalings in a wide-gap turbulent Taylor–Couette flow. *J. Fluid Mech.* **831**, 330–357.

Girifalco, L.A. & Good, R.J. 1957 A theory for the estimation of surface and interfacial energies. I. Derivation and application to interfacial tension. *J. Phys. Chem.* **61** (7), 904–909.

Gopalan, B. & Katz, J. 2010 Turbulent shearing of crude oil mixed with dispersants generates long microthreads and microdroplets. *Phys. Rev. Lett.* **104** (5), 054501.

Grossmann, S., Lohse, D. & Sun, C. 2016 High–Reynolds number Taylor–Couette turbulence. *Annu. Rev. Fluid Mech.* **48** (1), 53–80.

Hinze, J.O. 1955 Fundamentals of the hydrodynamic mechanism of splitting in dispersion processes. *AICHE J.* **1** (3), 289–295.

Hori, N., Ng, C.S., Lohse, D. & Verzicco, R. 2023 Interfacial-dominated torque response in liquid–liquid Taylor–Couette flows. *J. Fluid Mech.* **956**, A15.

Huisman, S.G., van Gils, D.P.M., Grossmann, S., Sun, C. & Lohse, D. 2012*a* Ultimate turbulent Taylor–Couette flow. *Phys. Rev. Lett.* **108** (2), 024501.

Huisman, S.G., van Gils, D.P.M. & Sun, C. 2012*b* Applying laser Doppler anemometry inside a Taylor–Couette geometry using a ray-tracer to correct for curvature effects. *Eur. J. Mech. B/Fluids* **36**, 115–119.

Huisman, S.G., Lohse, D. & Sun, C. 2013*a* Statistics of turbulent fluctuations in counter-rotating Taylor–Couette flows. *Phys. Rev. E* **88** (6), 063001.

Huisman, S.G., Scharnowski, S., Cierpka, C., Kähler, C.J., Lohse, D. & Sun, C. 2013*b* Logarithmic boundary layers in strong Taylor–Couette turbulence. *Phys. Rev. Lett.* **110** (26), 264501.

Ibarra, R., Matar, O.K. & Markides, C.N. 2021 Experimental investigations of upward-inclined stratified oil-water flows using simultaneous two-line planar laser-induced fluorescence and particle velocimetry. *Intl J. Multiphase Flow* **135**, 103502.

Ibarra, R., Zadrazil, I., Matar, O.K. & Markides, C.N. 2018 Dynamics of liquid–liquid flows in horizontal pipes using simultaneous two–line planar laser–induced fluorescence and particle velocimetry. *Intl J. Multiphase Flow* **101**, 47–63.

Kilpatrick, P.K. 2012 Water-in-crude oil emulsion stabilization: review and unanswered questions. *Energy Fuels* **26** (7), 4017–4026.

Kokal, S. 2005 Crude-oil emulsions: a state-of-the-art review. *SPE Prod. Facilities* **20** (01), 5–13.

Kolmogorov, A.N. 1949 On the disintegration of drops by turbulent flows. *Dokl. Akad. Nauk SSSR* **66**, 825–828.

Kumara, W.A.S., Halvorsen, B.M. & Melaaen, M.C. 2010 Particle image velocimetry for characterizing the flow structure of oil–water flow in horizontal and slightly inclined pipes. *Chem. Engng Sci.* **65** (15), 4332–4349.

Kurtz Jr., S.S. & Ward, A.L. 1936 The refractivity intercept and the specific refraction equation of Newton. I. development of the refractivity intercept and comparison with specific refraction equations. *J. Franklin Inst.* **222** (5), 563–592.

Lee, L.H. 1993 Scope and limitations of the equation of state approach for interfacial tensions. *Langmuir* **9** (7), 1898–1905.

Lemenand, T., Della Valle, D., Dupont, P. & Peerhossaini, H. 2017 Turbulent spectrum model for drop-breakup mechanisms in an inhomogeneous turbulent flow. *Chem. Engng Sci.* **158**, 41–49.

LEVICH, V.G. 1962 *Physicochemical Hydrodynamics*. Prentice-Hall Inc.

LI, M. & GARRETT, C. 1998 The relationship between oil droplet size and upper ocean turbulence. *Mar. Pollut. Bull.* **36** (12), 961–970.

MANDAL, A., SAMANTA, A., BERA, A. & OJHA, K. 2010 Characterization of oil–water emulsion and its use in enhanced oil recovery. *Ind. Engng Chem. Res.* **49** (24), 12756–12761.

MCCLEMENTS, D.J. 2004 *Food Emulsions: Principles, Practices, and Techniques*. CRC.

MORGAN, R.G., MARKIDES, C.N., ZADRAZIL, I. & HEWITT, G.F. 2013 Characteristics of horizontal liquid–liquid flows in a circular pipe using simultaneous high-speed laser-induced fluorescence and particle velocimetry. *Intl J. Multiphase Flow* **49**, 99–118.

MUKHERJEE, S., SAFDARI, A., SHARDT, O., KENJEREŠ, S. & VAN DEN AKKER, H.E.A. 2019 Droplet–turbulence interactions and quasi-equilibrium dynamics in turbulent emulsions. *J. Fluid Mech.* **878**, 221–276.

NEWTON, I. 1704 *Opticks: Or, A treatise of the reflections, refractions, inflexions and colours of light*.

NI, R. 2024 Deformation and breakup of bubbles and drops in turbulence. *Annu. Rev. Fluid Mech.* **56** (1), 319–347.

PERLEKAR, P. 2019 Kinetic energy spectra and flux in turbulent phase-separating symmetric binary-fluid mixtures. *J. Fluid Mech.* **873**, 459–474.

PERLEKAR, P., BENZI, R., CLERCX, H.J.H., NELSON, D.R. & TOSCHI, F. 2014 Spinodal decomposition in homogeneous and isotropic turbulence. *Phys. Rev. Lett.* **112** (1), 014502.

PERLEKAR, P., BIFERALE, L., SBRAGAGLIA, M., SRIVASTAVA, S. & TOSCHI, F. 2012 Droplet size distribution in homogeneous isotropic turbulence. *Phys. Fluids* **24** (6), 065101.

PIELA, K., DELFOS, R., OOMS, G., WESTERWEEL, J. & OLIEMANS, R.V.A. 2008 On the phase inversion process in an oil–water pipe flow. *Intl J. Multiphase Flow* **34** (7), 665–677.

POPE, S.B. 2000 *Turbulent Flows*. Cambridge University Press.

PROCACCIA, I., CHING, E.S.C., CONSTANTIN, P., KADANOFF, L.P., LIBCHABER, A. & WU, X.-Z. 1991 Transitions in convective turbulence: the role of thermal plumes. *Phys. Rev. A* **44** (12), 8091–8102.

REIS, J.C.R., LAMPREIA, I.M.S., SANTOS, Â.F.S., MOITA, M.L.C.J. & DOUHÉRET, G. 2010 Refractive index of liquid mixtures: theory and experiment. *Chem. Phys. Chem.* **11** (17), 3722–3733.

RISSO, F. & FABRE, J. 1998 Oscillations and breakup of a bubble immersed in a turbulent field. *J. Fluid Mech.* **372**, 323–355.

ROCCON, A., DE PAOLI, M., ZONTA, F. & SOLDATI, A. 2017 Viscosity-modulated breakup and coalescence of large drops in bounded turbulence. *Phys. Rev. Fluids* **2** (8), 083603.

ROSTI, M.E., GE, Z., JAIN, S.S., DODD, M.S. & BRANDT, L. 2019 Droplets in homogeneous shear turbulence. *J. Fluid Mech.* **876**, 962–984.

SHANG, X.-D., QIU, X.-L., TONG, P. & XIA, K.-Q. 2003 Measured local heat transport in turbulent Rayleigh–Bénard convection. *Phys. Rev. Lett.* **90** (7), 074501.

SPERNATH, A. & ASERIN, A. 2006 Microemulsions as carriers for drugs and nutraceuticals. *Adv. Colloid Interface Sci.* **128**, 47–64.

SU, J., WANG, C., ZHANG, Y.-B., XU, F., WANG, J. & SUN, C. 2024*a* Turbulence modulation in liquid–liquid two-phase Taylor–Couette turbulence. *J. Fluiid Mech.* **999**, A98.

SU, J., YI, L., ZHAO, B., WANG, C., XU, F., WANG, J. & SUN, C. 2024*b* Numerical study on the mechanism of drag modulation by dispersed drops in two-phase Taylor–Couette turbulence. *J. Fluiid Mech.* **984**, R3.

SU, J., ZHANG, Y.-B., WANG, C., YI, L., XU, F., FAN, Y., WANG, J. & SUN, C. 2025 How interfacial tension enhances drag in turbulent Taylor–Couette flow with neutrally buoyant and equally viscous droplets. *J. Fluid Mech.* **1002**, A2.

TREFFTZ-POSADA, P. & FERRANTE, A. 2023 On the interaction of Taylor length-scale size droplets and homogeneous shear turbulence. *J. Fluid Mech.* **972**, A9.

WANG, C., DEGROOT, C.T. & FLORYAN, J.M. 2023 Numerical simulation of drag reduction for turbulent flow in cylindrical annuli with axial corrugations. *Trans. Can. Soc. Mech. Engng* **48** (1), 164–172.

WANG, C., YI, L., JIANG, L. & SUN, C. 2022*a* How do the finite-size particles modify the drag in Taylor–Couette turbulent flow. *J. Fluid Mech.* **937**, A15.

WANG, C., YI, L., JIANG, L. & SUN, C. 2022*b* Turbulence drag modulation by dispersed droplets in Taylor–Couette flow: the effects of the dispersed phase viscosity. *J. Fluid Mech.* **952**, A39.

WIEDERSEINER, S., ANDREINI, N., EPELY-CHAUVIN, G. & ANCEY, C. 2011 Refractive-index and density matching in concentrated particle suspensions: a review. *Exp. Fluids* **50** (5), 1183–1206.

WRIGHT, S.F., ZADRAZIL, I. & MARKIDES, C.N. 2017 A review of solid–fluid selection options for optical-based measurements in single-phase liquid, two-phase liquid–liquid and multiphase solid–liquid flows. *Exp. Fluids* **58** (9), 1–39.

YAKHOT, V. 1989 Probability distributions in high-Rayleigh number Bénard convection. *Phys. Rev. Lett.* **63** (18), 1965–1967.

YI, L., GIROTTO, I., TOSCHI, F. & SUN, C. 2024 Divergence of critical fluctuations on approaching catastrophic phase inversion in turbulent emulsions. *Phys. Rev. Lett.* **133** (13), 134001.

YI, L., TOSCHI, F. & SUN, C. 2021 Global and local statistics in turbulent emulsions. *J. Fluid Mech.* **912**, A13.

YI, L., WANG, C., HUISMAN, S.G. & SUN, C. 2023 Recent developments of turbulent emulsions in Taylor–Couette flow. *Phil. Trans. R. Soc. A: Math. Phys. Engng Sci.* **381** (2243), 20220129.

YI, L., WANG, C., VAN VUREN, T., LOHSE, D., RISSO, F., TOSCHI, F. & SUN, C. 2022 Physical mechanisms for droplet size and effective viscosity asymmetries in turbulent emulsions. *J. Fluid Mech.* **951**, A39.

ZHANG, Y.-B., FAN, Y., SU, J., XI, H.-D. & SUN, C. 2025 Global drag reduction and local flow statistics in Taylor–Couette turbulence with dilute polymer additives. *J. Fluid Mech.* **1002**, A33.